

# Minority magnons and mode branching in monolayer Fe<sub>3</sub>GeTe<sub>2</sub>

Thorbjørn Skovhus<sup>1,\*</sup> and Thomas Olsen<sup>1</sup>

<sup>1</sup>*CAMD, Department of Physics, Technical University of Denmark, 2800 Kgs. Lyngby Denmark*

In this letter, we predict the existence of minority magnons in a monolayer of Fe<sub>3</sub>GeTe<sub>2</sub> using first principles calculations. Minority magnons constitute a new type of collective magnetic excitations which increase the magnetic moment rather than lower it, contrary to ordinary (majority) magnons. The presence of such quasi-particles is made possible by the nontrivial ferromagnetic band structure of Fe<sub>3</sub>GeTe<sub>2</sub> originating from its nonequivalent Fe sublattices. The result is a strong peak in the dynamic spin-raising susceptibility  $\chi^{-+}(\omega)$  in the long wavelength limit, which is the hallmark of minority magnon physics. We calculate the susceptibility using time-dependent density functional theory and perform a detailed mode analysis, which allows us to separate and investigate the individual magnon modes as well as the Stoner excitations that constitute the many-body spectrum. For minority as well as majority magnons, the analysis reveals a plethora of magnetic excitations, which in addition to the standard main magnon branches include both satellite, valley and spin-inversion magnons, originating from the itinerancy of the ferromagnetic order. The physics underlying this analysis is in no way restricted to Fe<sub>3</sub>GeTe<sub>2</sub>, and minority magnons are expected to be observable in many complex ferromagnetic materials.

In the quasi-particle picture, the excited states which alter the local direction of magnetization in magnetic crystals are referred to as magnons, each carrying a unit of spin angular momentum in the absence of spin-orbit coupling. Magnons are of a collective nature, that is, the alteration of the magnetization direction is mediated by a collection of correlated electrons, rather than of a single (dressed) electron-hole pair. The correlated nature of magnons makes for a challenging theoretical treatment, and the far majority of theoretical as well as experimental works rely on Heisenberg Hamiltonians to model and interpret magnetic excitations. In this picture, the magnetic structure is modelled in terms of localized magnetic moments coupled by exchange interactions, and the magnons can be obtained as eigenmodes in the spin-wave equation of motion (SWEOM) [1]. With a single localized moment per magnetic site, the spin-raising operator  $\hat{S}_i^+$  cannot be applied to sites  $i$  with the local spin aligned to the  $z$ -axis. Hence, the quantum mechanical SWEOM for a ferromagnet only includes modes which reduce  $S^z$ . However, when solved semi-classically, an additional set of eigenmodes that increase  $S^z$  appear at negative frequencies, constructed as linear combinations of  $S_i^+$ .

For metals, it is not obvious that the picture of localized moments remains valid, and indeed there are several well known itinerant electron effects, such as Stoner stripes and Landau damping, which cannot be described in the Heisenberg model [2–4]. Instead one needs an explicit treatment of the electronic bands, such as in the Stoner model. Here, a Hubbard model is treated in the mean field, resulting in a spin splitted band structure for certain ranges of parameters. Due to the spin splitting there exists a continuum of electron-hole pairs with opposite spin (Stoner pairs), which is gapped at zero momentum transfer. The magnons are modelled as coherent superpositions of the majority part of the continuum, that is, of the pairs where an electron has been transferred

from an occupied majority spin state to an unoccupied minority spin state, solving the Stoner equation of motion in the random phase approximation (RPA). In fact, the dispersion of the collective magnon mode can be extracted from the RPA susceptibility as poles on the real frequency axis situated in the gap below the Stoner continuum [5, 6]. In addition to the majority Stoner pairs, which lower  $S^z$ , the Stoner continuum can also include minority Stoner pairs involving an occupied minority spin state and an unoccupied majority spin state, thus raising  $S^z$ . In a single-band model like the spin-polarized homogeneous electron gas, minority Stoner pairs only exist for wave vectors large enough to connect the majority and minority Fermi surfaces. As a result, there is no gap below the minority Stoner continuum in which a collective magnon mode can exist. However, in a multi-band model of ferromagnetism, there is nothing to prohibit the existence of such a minority magnon mode, given that the ferromagnet has at least one fully occupied minority  $d$ -band as well as majority  $d$ -states above the Fermi level.

In this letter, we showcase how minority magnons enter the first principles theory of linear response and predict the presence of such magnons in the itinerant ferromagnetic monolayer Fe<sub>3</sub>GeTe<sub>2</sub> [7]. This compound has recently spurred significant interest due to gate-tunable Curie temperature (exceeding room temperature) as well as efficient spin-orbit torque switching [8, 9] making it a highly promising venue for 2D spintronics applications. The presence of three Fe atoms (two of which are equivalent) in the unit cell implies a rich electronic structure and, as we will see, gives rise to minority magnon excitations. We base our analysis on calculations of the Fe<sub>3</sub>GeTe<sub>2</sub> susceptibility within the adiabatic local density approximation (ALDA) to linear response time-dependent density functional theory (LR-TDDFT) [2, 4, 10–12]. In addition to the presence of minority magnons, we also provide a detailed account of the pro-

nounced mode branching of the optical majority modes in  $\text{Fe}_3\text{GeTe}_2$ .

For ferromagnets with vanishing spin-orbit coupling, a weakly perturbing transverse magnetic field induces a transverse magnetization without coupling to the longitudinal degrees of freedom [2, 4]. With the ground state spin-polarized along the positive  $z$ -direction,

$$\delta n^\alpha(\mathbf{r}, t) = \sum_{\beta} \int_{-\infty}^{\infty} dt' \int d\mathbf{r}' \chi^{\alpha\beta}(\mathbf{r}, \mathbf{r}', t - t') W_{\text{ext}}^\beta(\mathbf{r}', t'), \quad (1)$$

where  $n^\alpha$  is the transverse electron spin-density,  $\alpha, \beta \in \{x, y\}$ , and  $\mathbf{W}_{\text{ext}} = \mu_B \mathbf{B}_{\text{ext}}$ . Crucially, the four entries of the transverse magnetic susceptibility can be decomposed into circular coordinates,

$$\chi^{[x,y]} = \begin{pmatrix} \chi^{+-} + \chi^{-+} & i\chi^{+-} - i\chi^{-+} \\ -i\chi^{+-} + i\chi^{-+} & \chi^{+-} + \chi^{-+} \end{pmatrix}, \quad (2)$$

where  $\chi^{+-}(\omega)$  and  $\chi^{-+}(\omega)$  yield the response to negatively and positively circulating magnetic fields,  $\mathbf{B}_{\text{ext}}(\mathbf{r}, t) = B_{\text{ext}}(\mathbf{r})[\cos(\omega t)\mathbf{e}_x \mp \sin(\omega t)\mathbf{e}_y]$ . The inelastic part of the response to such fields is proportional to the scattering function  $S^{+-}(\omega)$  evaluated at positive and negative frequencies respectively [13, 14]. The scattering function can be decomposed into two distinct spectral functions [4]:

$$S^{+-}(\mathbf{r}, \mathbf{r}', \omega) = A^{+-}(\mathbf{r}, \mathbf{r}', \omega) - A^{-+}(\mathbf{r}', \mathbf{r}, -\omega). \quad (3)$$

These are spectral functions for the excited states  $|\alpha\rangle$  which decrease and increase  $S^z$  by  $\hbar$  respectively, weighted by the matrix elements  $n_{\alpha\alpha'}^\pm(\mathbf{r}) \equiv \langle \alpha | \hat{n}^\pm(\mathbf{r}) | \alpha' \rangle$ :

$$A^{+-}(\mathbf{r}, \mathbf{r}', \omega) = \sum_{\alpha > 0} n_{0\alpha}^+(\mathbf{r}) n_{\alpha 0}^-(\mathbf{r}') \delta(\hbar\omega - (E_\alpha - E_0)). \quad (4)$$

Here  $\hat{n}^+(\mathbf{r}) = \hat{\psi}_\uparrow^\dagger(\mathbf{r})\hat{\psi}_\downarrow(\mathbf{r})$ ,  $\hat{n}^-(\mathbf{r}) = \hat{\psi}_\downarrow^\dagger(\mathbf{r})\hat{\psi}_\uparrow(\mathbf{r})$  and  $\pm$  indices can be interchanged to yield  $A^{-+}$ . Thus, by definition any (bright) majority magnon will manifest itself as positive spectral weight in the scattering function  $S^{+-}$  at nonnegative frequencies, whereas minority magnons can provide negative spectral weight at negative frequencies.

Within the framework of LR-TDDFT, the many-body susceptibility  $\chi^{+-}$  can be obtained from the corresponding  $\chi_{\text{KS}}^{+-}$  of the noninteracting Kohn-Sham system by inverting a Dyson-like equation [11]. For the purpose of this letter, we have used a new implementation of the ALDA [15] in the GPAW linear response code [4, 16, 17], which enables us to accurately describe magnons in 2D materials. Here, the Fourier transform of the ALDA self-enhancement function,

$$\Xi_{\text{ALDA}}^{++}(\mathbf{r}, \mathbf{r}', \omega) = \chi_{\text{KS}}^{+-}(\mathbf{r}, \mathbf{r}', \omega) f_{\text{LDA}}^{-+}(\mathbf{r}'), \quad (5)$$

is calculated using the projector augmented wave method [18], and the Dyson equation is inverted in the plane-wave basis:

$$\chi^{+-}(\mathbf{q}, \omega) = [1 - \Xi^{++}(\mathbf{q}, \omega)]^{-1} \chi_{\text{KS}}^{+-}(\mathbf{q}, \omega). \quad (6)$$

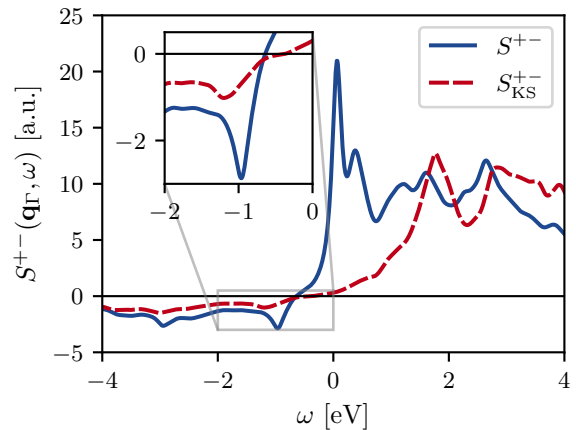


FIG. 1. Transverse magnetic scattering function for the many-body and Kohn-Sham systems in the long wavelength limit, with majority and minority excitations manifesting themselves at positive and negative frequencies respectively.

In previous implementations, the self-enhancement function was calculated in reciprocal space, which was highly problematic for 2D materials, since the LDA kernel diverges in vacuum. In contrast, the self-enhancement function is exponentially localized to the monolayer, making the Fourier transform hereof much more well behaved.

Our calculations takes the LDA ground state as a starting point. In this regard, we find that the two Fe(I) atoms carry a magnetic moment of  $2.39 \mu_B$  each, whereas the single Fe(II) atom has a reduced moment of  $1.36 \mu_B$  which can be rationalized based on the band structure and projected density of states [19]. In addition to the reduced moment, we identify in the band structure an almost flat minority band  $0.71$ – $0.83$  eV below the Fermi level, thus making monolayer  $\text{Fe}_3\text{GeTe}_2$  a promising candidate material to host minority magnons. In Fig. 1, we show the full trace of  $S^{+-}$  evaluated at  $\mathbf{q}_{\Gamma}$  and compare it to the scattering function of the Kohn-Sham system. At negative frequencies, we find the minority excitations.  $S_{\text{KS}}^{+-}$  displays a wide continuum of noninteracting minority Stoner pairs, which is gapped and exhibits a broad peak at its onset, due in part to the nondispersive minority band below the Fermi level [19]. In the many-body scattering function, electron correlations have resulted in a clear collective minority magnon peak below the main Stoner continuum. Interestingly, the correlation effects have actually enhanced the spectral weight across all the calculated negative frequencies. Since the zeroth moment of the scattering function is identical in the Kohn-Sham and many-body systems thanks to a sum rule [4, 20], this means that the total spectral weight at positive frequencies must have been increased as well. As we shall see, this is a consequence of the mutual collective enhancement of the majority and minority channels.

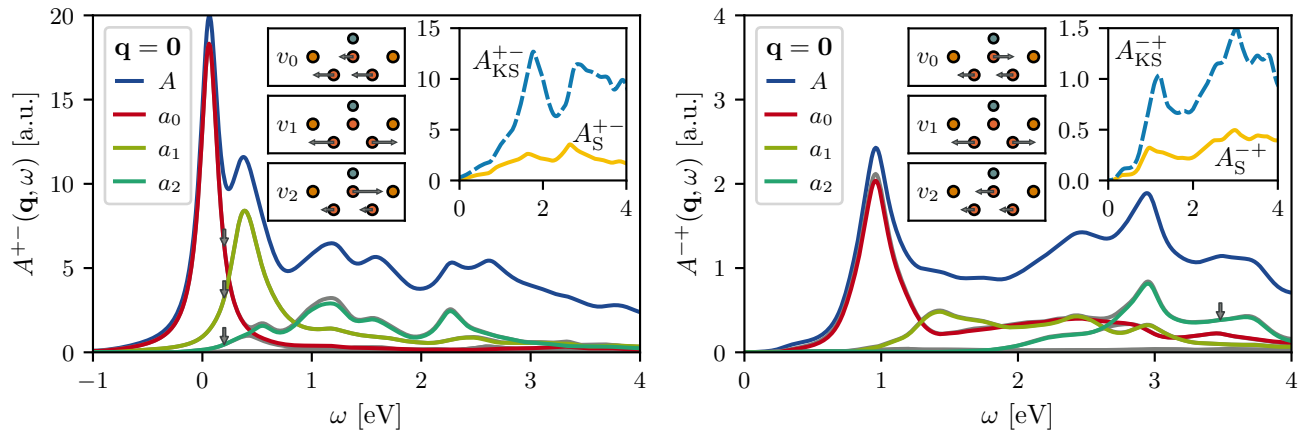


FIG. 2. Eigenvalue decomposition of the spectrum of majority (left) and minority (right) excitations in the long wavelength limit. The spectral function  $A(\mathbf{q}, \omega)$  (blue) is constructed as the sum of eigenvalues (grey), and the magnon lineshapes  $a_n(\mathbf{q}, \omega)$  are calculated as spectral projections onto magnon eigenvectors extracted at the shown frequency (vertical arrows). The magnon eigenmodes are shown in the central insets. In the upper right insets, the remaining many-body Stoner spectrum is compared to the spectral function of the Kohn-Sham system.

At the majority side of the Kohn-Sham scattering function, the Stoner continuum features two distinct peaks, rather than a single peak corresponding to a unique exchange splitting of the  $d$ -bands. For the many-body susceptibility, the optical magnon modes extend deeply into this region of frequencies, resulting in significant mode branching. As a consequence, the many-body scattering function in Fig. 1 has more than the three peaks at positive frequencies expected based on a Heisenberg model treatment (one for each Fe-atom).

To analyze each magnon mode independently, we separate the majority and minority spectral functions (4) according to Eq. (3), that is, in terms of the positive and negative eigenvalues of  $S^{+-}$  respectively. This allows us to extract individual mode lineshapes as shown in Fig. 2. In contrast to the Kohn-Sham spectrum, the many-body spectral functions exhibit exactly three eigenmodes with scattering amplitudes order(s) of magnitude larger than the rest (which are barely visible in Fig. 2). These are the collective magnon modes driven by the electronic correlations of the system. Apart from a difference in scattering amplitude, the picture is strikingly similar for the majority and minority channels, with the notable exception that only the majority spectrum includes a Goldstone mode. Instead, the minority mode with lowest energy is peaked around 0.96 eV in the long wavelength limit. Subtracting the lineshapes of the three collective magnon modes from the trace of the spectral function  $A(\omega)$ , one is left with the many-body Stoner spectrum  $A_S(\omega)$ . In Fig. 2, we compare this to the Kohn-Sham Stoner spectrum. The two spectra display remarkably identical features, meaning that the electronic correlations at the ALDA level only lead to a slight renormalization of the Stoner pairs.

Next, we will analyze the magnon mode enhancement from the Dyson equation (6) and categorize the different peaks observed within a single mode. Outside the Stoner continuum, the many-body susceptibility  $\chi^{+-}$  is pole-free, except for points where  $[1 - \Xi^{++}(\mathbf{q}, \omega)] \rightarrow 0$ . In fact,  $\Xi^{++}(\mathbf{r}, \mathbf{r}', t - t')$  encodes the induced transverse magnetization at time  $t$  and position  $\mathbf{r}$  due to the fluctuations in the transverse exchange-correlation field happening in response to a change in the magnetization at previous time  $t'$  and position  $\mathbf{r}'$ . Thus, if the self-enhancement function has an eigenvalue of unity, it entails the existence of a fluctuational eigenmode  $\delta n^\alpha(\mathbf{r}, \omega)$ , which is self-sustained via the effective electron-electron interaction and gives rise to a pole in the many-body susceptibility. This is what is understood as a coherent collective magnon resonance in the first principles theory. Inside the Stoner continuum, the eigenvalues of  $\Xi^{++}$  will also attain a finite imaginary part, in fact, the poles of  $\Xi^{++}$  and  $\chi_{KS}^{+-}$  are identical in the ALDA. Nevertheless, if the real part of a  $\Xi^{++}$  eigenvalue reaches unity, we can still categorize the corresponding magnon peak as coherent, but in this case with a finite lifetime due to Landau damping.

In Fig. 3, we analyze the different magnon enhancement scenarios arising in monolayer  $\text{Fe}_3\text{GeTe}_2$  by projecting the self-enhancement function onto the extracted magnon mode vectors,  $\xi_n(\mathbf{q}, \omega) = \langle v_n | \Xi(\mathbf{q}, \omega) | v_n \rangle$ . For the Goldstone ( $n = 0$ ) mode at  $\mathbf{q}_\Gamma$ , the Stoner spectrum consists of a single main peak in  $\text{Im} \xi_0^{++}(\omega)$  giving rise to a simple pole-like feature in  $\text{Re} \xi_0^{++}(\omega)$  via the Kramers-Kronig relation and an undamped coherent magnon resonance below the Stoner continuum in turn. At shorter wave lengths, the Stoner continuum extends to progressively lower frequencies and at the K-point the lineshape

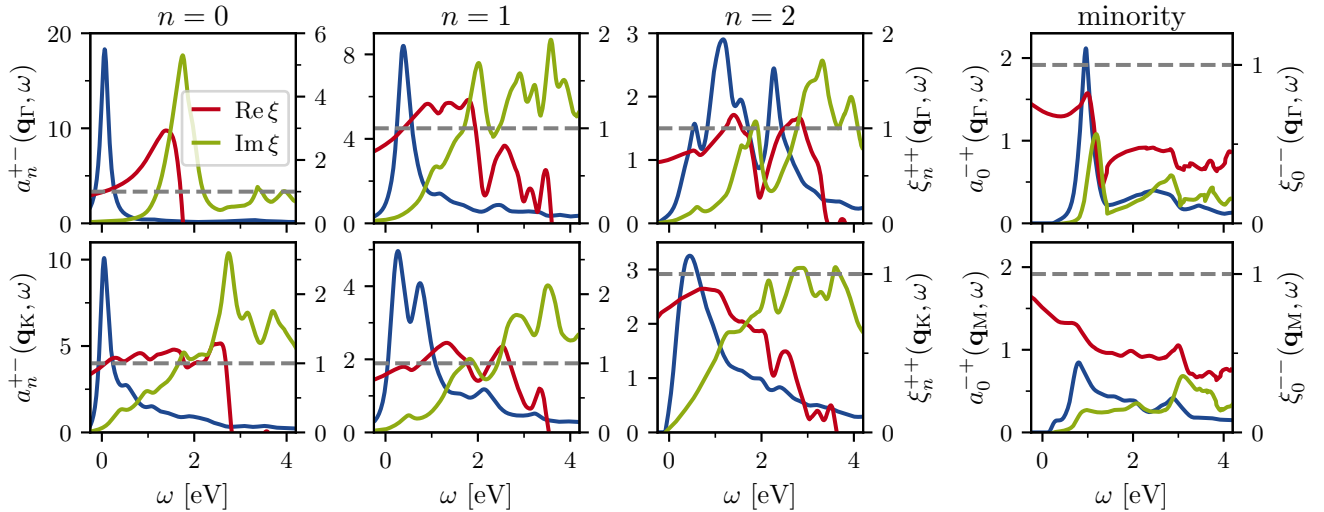


FIG. 3. Collective enhancement of the three majority and low energy minority magnon modes (left to right) in the long wavelength limit (top row) and at the  $K$  and  $M$  high-symmetry points (bottom row). The magnon lineshapes  $a_n(\mathbf{q}, \omega)$  (left axis in blue) are the result of an enhancement factor of  $[1 - \text{Re } \xi_n(\mathbf{q}, \omega)]^{-1}$ , where  $\xi_n$  (right axis in red and green for the real and imaginary parts) is the projection of the magnon mode onto the corresponding self-enhancement function.

has undergone Landau damping, acquiring a long tail with several small Stoner features. Despite the damping, the magnon peak has just barely remained coherent in the sense that  $\text{Re } \xi_0^{++}(\omega)$  crosses unity at the peak position, in contrast to e.g. the  $n = 2$  majority mode at the  $K$ -point. For the minority magnon mode, the picture is, once again, very similar. A single well-defined peak in the Stoner spectrum creates a pole-like feature in  $\text{Re } \xi_0^{--}(\omega)$  which results in the collective enhancement of a magnon peak at the lower end of the continuum. For the  $\text{Fe}_3\text{GeTe}_2$  monolayer, the minority Stoner spectrum lacks the sufficient amplitude to produce a coherent minority resonance. However, one may notice that  $\text{Re } \xi_0^{--}(\omega)$  does not proceed to vanish below the Stoner continuum, but increases instead thanks to the overlap with the  $n = 2$  majority mode. This implies that the majority Stoner continuum contributes constructively to the minority magnon enhancement, which is essential in order to explain the relative near-coherency of the minority magnon despite the limited density of unoccupied majority  $d$ -states in  $\text{Fe}_3\text{GeTe}_2$  [19]. In fact, had the low energy minority mode overlapped with the acoustic  $n = 0$  majority mode, for which  $\text{Re } \xi_0^{++}(\mathbf{q}_\Gamma, \omega = 0) = 1$ , the minority Stoner continuum depicted in Fig. 3 would indeed have been intense enough to produce a coherent minority resonance. For the optical majority magnon modes, we identify in Fig. 3 two main reasons for the wealth of peaks observed in the spectrum (mode branching). The first is due to Stoner satellites (sometimes also referred to as Stoner stripes [3, 4]). Glancing at the  $n = 1$  mode at  $\mathbf{q}_K$ , a Stoner satellite peak sits below the main continuum, generating an extra wiggle in  $\text{Re } \xi_1^{++}(\omega)$  and a

corresponding peak in the magnon lineshape below the satellite. Peaks of this sort, we categorize as satellite magnons. The second is due to cases where there are more than a single main Stoner peak, such as for the optical majority modes at  $\mathbf{q}_\Gamma$ . In this scenario, a magnon branch can reside in the valley in between two Stoner peaks, both as a coherent ( $n = 2$ ) and an incoherent ( $n = 1$ ) magnon resonance. These peaks are categorized as valley magnons, and due to Landau damping we often find that the lineshape is peaked further towards the bottom of the Stoner valley than what the real part of the self-enhancement function would suggest.

Following this procedure, we have computed the full scattering function as a function of wave vector  $\mathbf{q}$ , extracted the majority and minority magnon lineshapes and analyzed the self-enhancement function in order to categorize each of the magnon peaks. In Fig. 4, we present the resulting magnon branches of the  $n = 0$  minority magnon mode. We see that the main branch attains its largest scattering amplitude close to the  $\Gamma$ -point, where the resonance nearly is coherent, while it gets progressively damped as the corresponding Stoner peak is broadened for finite  $\mathbf{q}$ . Near the BZ boundary, where wave vectors  $\mathbf{q}$  connect the majority and minority Fermi surfaces, the branch is further damped from below due to spin-inverted majority Stoner pairs [21]. These are the pairs that give rise to the conventional minority scattering observed in the homogeneous electron gas [3], and at the  $K$ -point the corresponding spin-inversion magnon completely dominates the low energy spectrum to which the main branch becomes a shoulder in the lineshape. In the Supplemental Material [19], we provide analogous

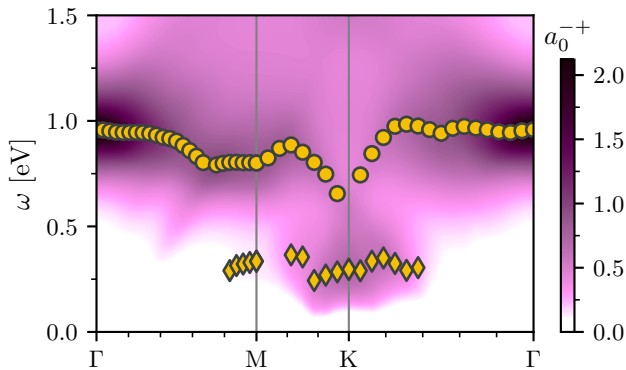


FIG. 4. Magnon band structure for the low energy minority magnon mode. The magnon mode lineshape  $a_0^{-+}(\mathbf{q}, \omega)$  is shown as a colored contour on top of which the peak positions of the identified magnon branches are shown. The main minority branch is marked with disks and the spin-inversion magnon branch with rhombuses.

band structure figures for the majority magnon modes and compare our results in this regard to a previous RPA study [22] of the majority modes as well as the spin-wave dispersion within the Heisenberg model calculated using magnetic force theorem exchange parameters [23–25].

In conclusion, we have showcased how minority magnon excitations enter the first principles theory of linear response and shown that monolayer  $\text{Fe}_3\text{GeTe}_2$  hosts three such collective modes in the ALDA. Along with the pronounced mode branching of the optical majority modes, we have studied the lowest energy minority magnon mode in detail. Despite the low density of unoccupied majority Fe  $d$ -states, we have found it to yield a nearly coherent minority magnon resonance close to the  $\Gamma$ -point. Based on these findings, we believe the experimental discovery of minority magnons in  $\text{Fe}_3\text{GeTe}_2$  or similar nontrivial ferromagnets to be eminent.

\* thosk@dtu.dk

- [1] S. V. Halilov, H. Eschrig, A. Y. Perlov, and P. M. Oppeneer, *Physical Review B* **58**, 293 (1998).
- [2] P. Buczek, A. Ernst, and L. M. Sandratskii, *Physical Review B* **84**, 174418 (2011).
- [3] C. Friedrich, M. C. T. D. Müller, and S. Blügel, in *Handbook of Materials Modeling: Methods: Theory and Modeling*, edited by W. Andreoni and S. Yip (Springer International Publishing, Cham, 2020) pp. 919–956.
- [4] T. Skovhus and T. Olsen, *Physical Review B* **103**, 245110 (2021).
- [5] T. Moriya, *Spin Fluctuations in Itinerant Electron Magnetism*, Springer Series in Solid-State Sciences, Vol. 56 (Springer-Verlag Berlin Heidelberg, 1985).
- [6] K. Yosida, *Theory of Magnetism*, Springer Series in Solid-State Sciences, Vol. 122 (Springer-Verlag Berlin Heidelberg, 1996).
- [7] Z. Fei, B. Huang, P. Malinowski, W. Wang, T. Song, J. Sanchez, W. Yao, D. Xiao, X. Zhu, A. F. May, W. Wu, D. H. Cobden, J.-H. Chu, and X. Xu, *Nature Materials* **17**, 778 (2018), 1803.02559.
- [8] M. Alghamdi, M. Lohmann, J. Li, P. R. Jothi, Q. Shao, M. Aldosary, T. Su, B. P. Fokwa, and J. Shi, *Nano Letters* **19**, 4400 (2019), 1903.00571.
- [9] H. Wang, H. Wu, J. Zhang, Y. Liu, D. Chen, C. Pandey, J. Yin, D. Wei, N. Lei, S. Shi, H. Lu, P. Li, A. Fert, K. L. Wang, T. Nie, and W. Zhao, *Nature Communications* **14**, 5173 (2023).
- [10] E. Runge and E. K. U. Gross, *Physical Review Letters* **52**, 997 (1984).
- [11] E. K. U. Gross and W. Kohn, *Physical Review Letters* **55**, 2850 (1985).
- [12] S. Y. Savrasov, *Physical Review Letters* **81**, 2570 (1998).
- [13] L. Van Hove, *Physical Review* **95**, 1374 (1954).
- [14] J. Jensen and A. R. Mackintosh, *Rare Earth Magnetism: Structures and excitations*, The International Series of Monographs on Physics (Clarendon Press, Oxford, 1991).
- [15] The details of the implementation will be documented elsewhere.
- [16] J. Yan, J. J. Mortensen, K. W. Jacobsen, and K. S. Thygesen, *Physical Review B* **83**, 245122 (2011).
- [17] J. J. Mortensen, A. H. Larsen, M. Kuisma, A. V. Ivanov, A. Taghizadeh, A. Peterson, A. Haldar, A. O. Dohn, C. Schäfer, E. Ö. Jónsson, E. D. Hermes, F. A. Nilsson, G. Kastlunger, G. Levi, H. Jónsson, H. Häkkinen, J. Fojt, J. Kangsabanik, J. Sødequist, J. Lehtomäki, J. Heske, J. Enkovaara, K. T. Winther, M. Dulak, M. M. Melander, M. Ovesen, M. Louhivuori, M. Walter, M. Gjerding, O. Lopez-Acevedo, P. Erhart, R. Warmbier, R. Würdemann, S. Kaappa, S. Latini, T. M. Boland, T. Bligaard, T. Skovhus, T. Susi, T. Maxson, T. Rossi, X. Chen, Y. L. A. Schmerwitz, J. Schiøtz, T. Olsen, K. W. Jacobsen, and K. S. Thygesen, *Gpaw: open python package for electronic-structure calculations* (2023), arXiv:2310.14776 [cond-mat.mtrl-sci].
- [18] P. E. Blöchl, *Physical Review B* **50**, 17953 (1994).
- [19] See supplemental material at [url] for computational details as well as figures and discussion regarding the crystal structure, electronic band structure, projected density of states and majority magnon band structure.
- [20] B. Rousseau, A. Eiguren, and A. Bergara, *Physical Review B* **85**, 054305 (2012).
- [21] T. Skovhus, *Magnetic excitations from first principles*, Ph.D. thesis, Department of Physics, Technical University of Denmark (2021).
- [22] M. Costa, N. M. R. Peres, J. Fernández-Rossier, and A. T. Costa, *Physical Review B* **102**, 014450 (2020).
- [23] A. Liechtenstein, M. Katsnelson, V. Antropov, and V. Gubanov, *J. Magn. Magn. Mater.* **67**, 65 (1987).
- [24] P. Bruno, *Phys. Rev. Lett.* **90**, 087205 (2003).
- [25] F. L. Durhuus, T. Skovhus, and T. Olsen, *J. Phys. Condens. Matter* **35**, 105802 (2023).
- [26] S. Haastrup, M. Strange, M. Pandey, T. Deilmann, P. S. Schmidt, N. F. Hinsche, M. N. Gjerding, D. Torelli, P. M. Larsen, A. C. Riis-Jensen, J. Gath, K. W. Jacobsen, J. J. Mortensen, T. Olsen, and K. S. Thygesen, *2D Materials* **5**, 042002 (2018).
- [27] M. N. Gjerding, A. Taghizadeh, A. Rasmussen, S. Ali, F. Bertoldo, T. Deilmann, N. R. Knøsgaard, M. Kruse, A. H. Larsen, S. Manti, T. G. Pedersen, U. Petralanda,



- T. Skovhus, M. K. Svendsen, J. J. Mortensen, T. Olsen, and K. S. Thygesen, 2D Materials **8**, 044002 (2021).  
 [28] N. Singh, P. Elliott, T. Nautiyal, J. K. Dewhurst, and S. Sharma, Physical Review B **99**, 035151 (2019).

- [29] S. Lounis, A. T. Costa, R. B. Muniz, and D. L. Mills, Physical Review B **83**, 035109 (2011).

## Supplemental Material

### COMPUTATIONAL DETAILS

Studying the transverse magnetic excitations of monolayer  $\text{Fe}_3\text{GeTe}_2$ , we have used the relaxed crystal structure from the Computational 2D Materials Database C2DB [26, 27], adjusting the vacuum to 10 Å (see also Figs. 5 and 6). We calculate the LDA ground state on a  $48 \times 48 \times 1$   $\Gamma$ -centered  $k$ -point grid, based on which  $\chi_{\text{KS}}^{+-}$  and  $\Xi_{\text{ALDA}}^{++}$  is calculated using 12 empty-shell bands per atom, a plane-wave cutoff of 500 eV and a spectral broadening of 100 meV. Inverting the Dyson equation, we obtain  $\chi^{+-}$ , from which the scattering function  $S^{+-}$  is extracted as the anti-Hermitian part in the plane-wave components.

In order to analyze the magnon modes independently, see e.g. Fig. 2 of the main text, we reduce  $S^{+-}$  to a plane-wave cutoff of 200 eV, diagonalize it and save the 27 and 15 largest eigenvalues of  $A^{+-}$  and  $A^{-+}$  respectively, along with the corresponding eigenvectors and full eigenvalue trace. The basis reduction is basically a disk space saving exercise due to the need of running the calculations across many different jobs. We save also an eigendecomposition of the self-enhancement function consisting of its 42 largest eigenvalues, such that we can reconstruct both  $A^{+-}(\mathbf{q}, \omega)$ ,  $A^{-+}(\mathbf{q}, \omega)$  and  $\Xi^{++}(\mathbf{q}, \omega)$  after all calculations have finished. Apart from  $S^{+-}$ ,  $S_{\text{KS}}^{+-}$ ,  $A_{\text{KS}}^{+-}$  and  $A_{\text{KS}}^{-+}$  in Figs. 1 and 2 of main text (which are shown in the full 500 eV cutoff basis) all re-

sults of the letter are based on the reduced eigendecompositions in the 200 eV basis. From the spectral eigendecompositions, we extract the magnon lineshapes as the inner product  $a_n(\mathbf{q}, \omega) = \langle v_n | A(\mathbf{q}, \omega) | v_n \rangle$ , using magnon eigenvectors  $|v_n\rangle$  taken at a single frequency  $\omega$ . For the majority magnon modes, we choose  $\omega$  to maximize the minimum eigenvalue difference between the three modes:  $\max_{\omega} (\min_{n>0} [\lambda_{n-1}(\omega) - \lambda_n(\omega)])$ . This ensures the extraction of well-defined lineshapes, since the eigenvectors are only sensitive to the frequency in the vicinity of crossing eigenvalues. For the minority magnons, we focus in the letter on the lowest energy mode, extracting its mode vector at the eigenvalue maximum. The only exception is Fig. 2 of the main text, where we showcase that also the three minority magnon mode lineshapes can be extracted in a similar fashion to the majority modes, albeit a little less convincingly so since the  $n = 2$  mode does not extend to lower frequencies than 2 eV.

### BAND STRUCTURE AND PROJECTED DENSITY OF STATES

In Fig. 6, we show the LDA band structure and projected density of states of monolayer  $\text{Fe}_3\text{GeTe}_2$ . The reason for the reduced Fe(II) magnetic moment is found below the Fermi level, where there are several weakly dispersive minority bands with roughly equal weight on the  $d$ -orbitals of the Fe(I) and Fe(II) atoms, regardless of the fact that there are two of the former. As described in the main text, the near-coherent minority magnon mode arises due to a peak at the onset of the minority Stoner continuum  $S_{\text{KS}}^{+-}(\mathbf{q}, \omega)$ , situated around  $-1.2$  eV for  $\mathbf{q} = \mathbf{0}$ . Based on the projected density of states, it seems that the main supplier of holes to these specific minority Stoner pairs come from the nondispersive minority band 0.71–0.83 eV below the Fermi level and the minority band which lies rather nondispersively just below it at the M-point, 0.99 eV below the Fermi level. The majority electrons of the Stoner pairs are supplied by the small selection of bands with  $d$ -orbital weight that penetrate the Fermi level. Again, the main peak in the projected density of states arise due to a band which is rather nondispersive around the M-point, 0.25 eV above the Fermi level.

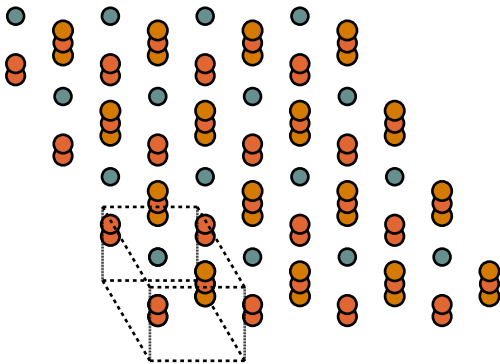


FIG. 5. Top view of the  $\text{Fe}_3\text{GeTe}_2$  monolayer crystal. For a side view, see Fig. 6.

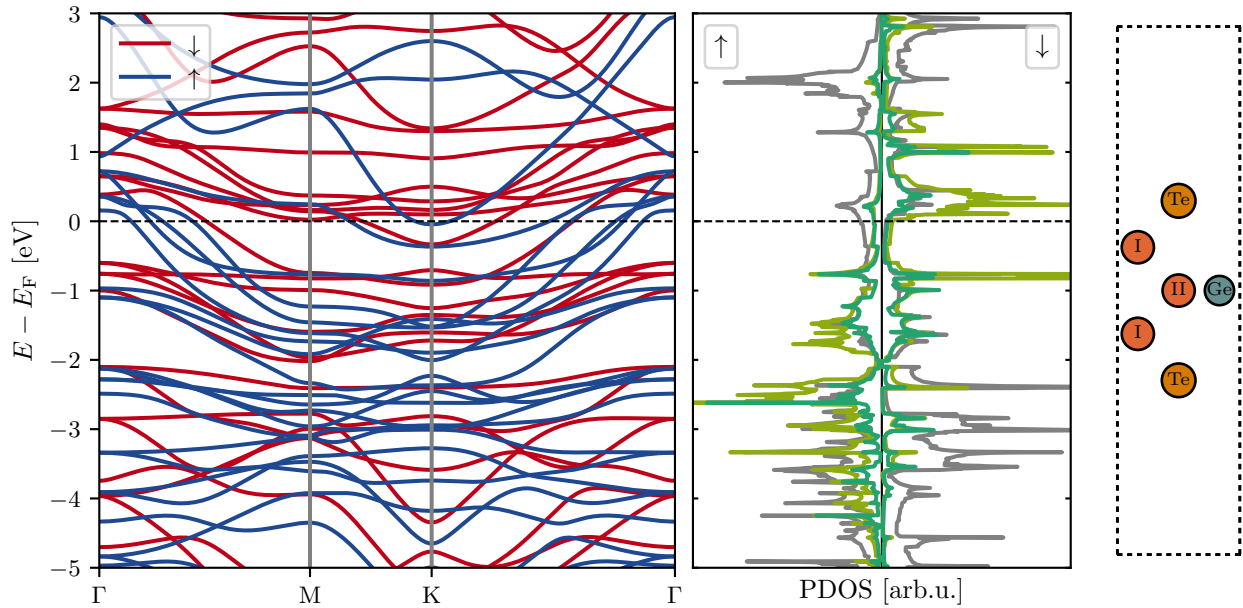


FIG. 6. LDA band structure and projected density of states of the  $\text{Fe}_3\text{GeTe}_2$  monolayer, as well as a side view of the unit cell. Projections onto Fe(I)  $d$ -orbitals are depicted in green, Fe(II)  $d$ -orbitals in teal and the remaining density of states in grey.

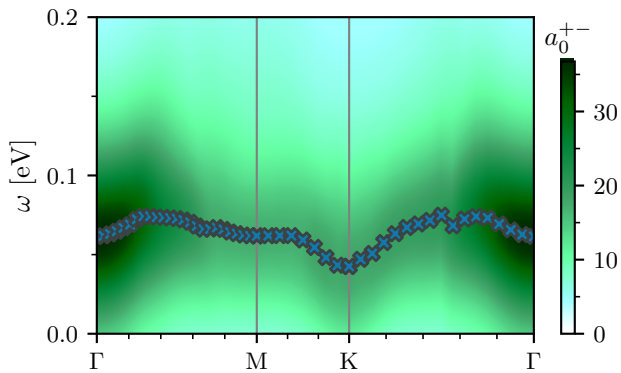


FIG. 7. Magnon band structure for the acoustic majority mode. The lineshape  $a_0^{+-}(\mathbf{q}, \omega)$  (color contour) was calculated with a reduced broadening of 50 meV, and the peak positions of the coherent Goldstone branch is shown with crosses.

### MAJORITY MAGNON BAND STRUCTURES

In Figs. 7 and 8, we present the magnon band structures of the majority modes in monolayer  $\text{Fe}_3\text{GeTe}_2$ . For the acoustic Goldstone mode, we show the raw ALDA dispersion with an observed gap error of 61 meV. Normally, one would correct this error by applying a rigid shift to the frequency axis [4, 28] or by using one of a series of more comprehensive correction schemes [2, 20, 29]. Regardless, we have not been able to converge the acoustic magnon dispersion within current computational constraints, why we have devoted our focus to the converged

minority and optical majority magnon modes instead. It should, however, be mentioned in passing, that with a plane-wave cutoff of 500 eV as shown in Fig. 7, the ALDA magnon dispersion suggests the ferromagnetic state to be dynamically unstable, since the minimum of the dispersion lies at the K-point rather than at the  $\Gamma$ -point. For the  $n = 1$  optical mode at the  $\Gamma$ -point, see Fig. 8, there are two main branches: a conventional coherent magnon branch around 390 meV and an incoherent valley magnon around 2.45 eV. Approaching the BZ edge, the valley magnon becomes coherent, whereas the conventional optical magnon branch splits in two, of which the lower one is categorized as a satellite magnon. In a previous RPA study of the magnon spectrum in monolayer  $\text{Fe}_3\text{GeTe}_2$  [22], the  $n = 1$  optical mode has been characterized as “nonbonding” (in a sublattice sense) since it only carries weight on the two Fe(I) atoms, see Fig. 2 of the main text. In that study, only the lower magnon branch was extracted (following what we assume to be the satellite magnon), and the existence of coherent high-frequency magnon resonances was overlooked. Where they find a relatively flat magnon dispersion with a bandwidth of  $\simeq 50$  meV, we find a bandwidth (following the satellite magnon) of 175 meV, in both cases dispersing to lower frequencies away from the  $\Gamma$ -point and centered around 300 meV. Lastly, for the  $n = 2$  optical magnon mode, we find two coherent branches at the  $\Gamma$ -point—a conventional magnon branch and a valley magnon, with satellite magnons below and in between, see also Fig. 3 of the main text. In the preceding RPA study [22], which is limited to frequencies up to 1 eV, no coherent

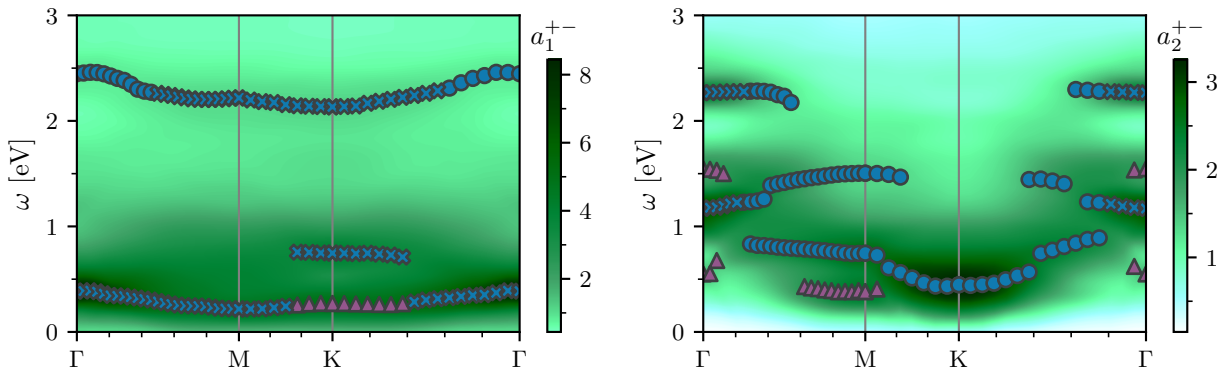


FIG. 8. Optical majority magnon band structure. The magnon mode lineshapes  $a_n^{+-}(\mathbf{q}, \omega)$  are shown as colored contour maps on top of which the peak positions of the identified magnon branches are shown. Peaks corresponding to a coherent magnon resonances are marked with crosses, incoherent magnon resonances with a disks and satellite magnons (which are all incoherent) with triangles.

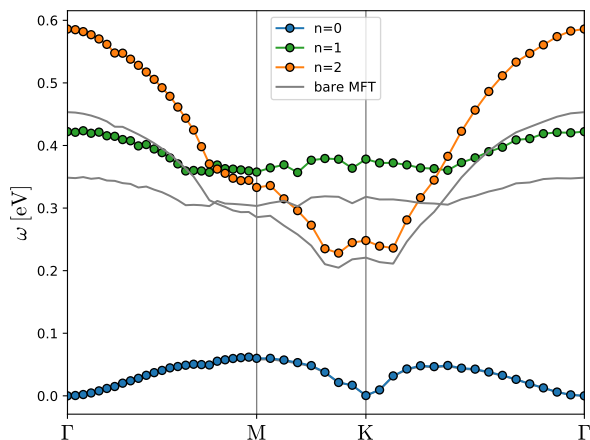


FIG. 9. Magnon dispersion obtained from linear response MFT. We show the results obtained with the renormalization scheme of Bruno [24] as well as the bare MFT results obtained from the original approach [23, 25].

branches corresponding to the  $n = 2$  mode are reported on. As the coherent branches disperse to higher frequencies and decohere away from the  $\Gamma$ -point, a new incoherent main branch appears at lower frequencies, with a satellite magnon branch at its foot around the M-point. Although it is not the focus of the RPA study [22], this lower main branch is clearly present in their data, but

seemingly with a slightly smaller bandwidth than the 460 meV we find here.

#### MAGNONS IN THE HEISENBERG MODEL

In Fig. 9 we show the magnon bands obtained from the magnetic force theorem (MFT) [23–25] using the same parameters as in the ALDA calculations. This approach enforces a Heisenberg description upon the magnetic structure and yields a distinct band (delta function lineshape) for each Fe atom in the unit cell. While one observes a dispersion reminiscent of the lowest magnon branch for each of the three modes obtained from ALDA, it is clear that this approach fails rather dramatically in providing a comprehensive description of the magnetic excitations. This is expected due to the rather complicated lineshapes that emerge throughout the Brillouin zone for both of the optical majority modes. In particular, for the  $n = 1$  mode the MFT approach follows the lowest branch on the entire path, although this becomes a satellite in the vicinity of the K-point. The  $n = 2$  mode on the other hand is incoherent in most of the Brillouin zone and the magnon energy is underestimated by a factor of two at K—probably due to the strong Landau damping, which is not accounted for in the Heisenberg description.